

# Quantum Monte Carlo study of systems interacting via long-range interactions mediated by a cavity

Marta Domínguez-Navarro , <sup>1, 2, \*</sup> Abel Rojo-Francàs , <sup>1, 2, 3, †</sup>  
 Bruno Juliá-Díaz , <sup>1, 2, ‡</sup> and Grigori E. Astrakharchik , <sup>4, §</sup>

<sup>1</sup>*Departament de Física Quàntica i Astrofísica, Facultat de Física,  
 Universitat de Barcelona, E-08028 Barcelona, Spain.*

<sup>2</sup>*Institut de Ciències del Cosmos, Universitat de Barcelona,  
 ICCUB, Martí i Franquès 1, E-08028 Barcelona, Spain.*

<sup>3</sup>*Quantum Systems Unit, Okinawa Institute of Science and Technology Graduate University,  
 Onna, Okinawa 904-0495, Japan.*

<sup>4</sup>*Departament de Física, Universitat Politècnica de Catalunya,  
 Campus Nord B4-B5, E-08034 Barcelona, Spain.*

We study one-dimensional quantum gases in continuous space with cavity-mediated infinite-range interactions using variational and diffusion Monte Carlo methods. Starting from the exact two-body solution, we construct a non-translationally invariant Jastrow wavefunction that accurately captures the spatial structure induced by the cavity field and provides an efficient many-body ansatz for both bosonic and fermionic systems. We analyze properties of three characteristic quantum systems, subject to long-range interactions: (i) ideal Bose gas (ii) interacting Bose gas (iii) ideal Fermi gas. In the absence of short-range interactions, we identify a crossover from a stable, weakly modulated phase realized for repulsive interactions to a delocalized bound state for attractive interactions, marked by clustering, loss of superfluidity, and the absence of a thermodynamic limit. Introducing short-range repulsion, either through contact interactions or fermionic statistics, leads to the formation of a mesoscopic gas-like regime that disappears in the thermodynamic limit. A qualitative phase diagram is proposed to illustrate the combined effects of short- and long-range interactions, highlighting the emergence of distinct regimes with characteristic structural properties.

## I. INTRODUCTION

The rapid development of quantum simulators has transformed the study of complex many-body phenomena by enabling their realization in highly controllable experimental platforms. Ultracold atomic gases [1] and trapped ions [2] offer unprecedented control over system parameters, facilitating the engineering of tailored quantum Hamiltonians and the exploration of exotic quantum phases [3, 4].

While short-range interactions are highly tunable and have been extensively studied, both theoretically [5, 6] and experimentally [7], more recently, long-range interactions have attracted sustained interest due to their distinct behavior and their capability of creating different types of orders simultaneously [8]. Theoretical studies have shown that long-range interactions can lead to phenomena such as supersolidity and non-equilibrium phase transitions, motivating ongoing efforts to explore their role in quantum many-body systems [9, 10]. Among the various schemes proposed to realize long-range interactions in quantum gases, high-finesse optical cavities offer a potent and versatile platform [11, 12]. Indeed, in these setups, atoms coherently scatter photons into a common cavity mode, resulting in effective infinite-range interac-

tions mediated by the light field. These interactions are highly tunable in both strength and symmetry and have been shown to drive phenomena such as self-organization [13], collective friction [14, 15], and symmetry-breaking phase transitions [16].

A key experimental realization of systems with long-range interactions was provided by Mottl et al. [17], who observed roton-like mode softening in the excitation spectrum of a Bose-Einstein condensate coupled to a standing-wave cavity. The divergence of the susceptibility at finite momentum was interpreted as a precursor to crystalline order. Such mode softening has been proposed as a possible route to supersolidity, where superfluid order coexists with long-range diagonal order (i.e. density modulation). Motivated by these early results, subsequent experiments have significantly broadened the scope of cavity Quantum Electrodynamics (QED). These include the realization of multimode cavities [18], the implementation of dynamically tunable optical lattices to explore driven phase transitions [19], and the development of programmable optomechanical arrays of levitated particles [20].

In addition to the experimental progress, theoretical studies aim at providing a comprehensive understanding of cavity-mediated long-range interactions. Effective models describing these systems often involve nonlocal and nonlinear couplings [13, 16, 21], which might require non-standard analytical and numerical approaches. In particular, mean-field and perturbative methods are generally inadequate in strongly interacting regimes. In this context, numerical techniques, especially Quantum

\* [mdominguez@icc.ub.edu](mailto:mdominguez@icc.ub.edu)

† [abel.rojo@oist.jp](mailto:abel.rojo@oist.jp)

‡ [bruno@fqa.ub.edu](mailto:bruno@fqa.ub.edu)

§ [grigori.astrakharchik@upc.edu](mailto:grigori.astrakharchik@upc.edu)

Monte Carlo (QMC) methods, offer a powerful non-perturbative framework for investigating ground-state properties and correlation functions in correlated quantum gases. Previous works have employed Monte Carlo methods to study cavity-mediated long-range interactions in lattice systems, specifically within extended Bose-Hubbard models [21, 22]. To the best of our knowledge, no exact solution was given to the many-body problem in continuum geometry.

The main goal of this work is to study the ground-state properties of a one-dimensional quantum gas with cavity-mediated long-range interactions, based on the ideas proposed in Ref. [17], by using a similar form of periodic infinite-ranged interactions. To obtain the ground-state properties of the many-body problem, we use Quantum Monte Carlo techniques, that is the variational and Diffusion Monte Carlo methods. We obtain accurate estimates of experimentally relevant observables such as the ground-state energy, density profiles, and static structure factor. We perform analysis of how the cavity-mediated interactions affect following three fundamental classes of quantum systems such as: (i) the ideal Bose gas, (ii) a weakly interacting Bose gas, (iii) a spinless ideal Fermi gas. This comparative approach enables us to identify how long-range correlations manifest differently depending on the underlying quantum statistics.

The structure of this work is as follows. In Section II, we introduce the physical context of the cavity setup and present the effective model Hamiltonian, together with the approximations used to reduce the system to a one-dimensional description, as well as outline the numerical techniques used, with particular attention to the construction of the trial wavefunctions and the implementation of the Monte Carlo algorithms. Building on these foundations, we present our first results in Sec. III, where we analyze the simple case of two particles to get a first look into the effects of the cavity-mediated interaction in a quantum system and to also use for the construction of the trial wavefunction in the many-body case. In Sec. IV, we extend the analysis to many-body systems of non-interacting bosons, characterizing the ground-state energy and density profiles for different number of particles. To further study the stability and properties of the long-range interaction in other systems, in Sec. V, we incorporate additional short-range physics, contact interactions for bosons, and Pauli's exclusion constraint for fermions, and study how these contributions affect the system's behavior in the presence of the long-range cavity potential. Finally, Sec. VI summarizes the main results obtained and future ventures.

## II. SYSTEM AND METHODS

In this section, we present the physical model that forms the basis of our numerical study. We begin by reviewing the key features of the experimental setup of Ref. [17], where ultracold atoms are coupled to a

single-mode optical cavity to realize tunable long-range interactions. We then introduce the full microscopic Hamiltonian describing the light-matter system, followed by a dimensional reduction leading to a simplified one-dimensional model in dimensionless units. This reduced model serves as the starting point for all subsequent numerical simulations.

Furthermore, we outline the numerical methods used throughout this work. Our approach consisted of three numerical methods: Imaginary Time Evolution (ITE) to extract the two-body wavefunction; Variational Monte Carlo (VMC) method to explore the many-body system using a variational ansatz based on the two-body solution; and Diffusion Monte Carlo (DMC) method to calculate exact estimates, within statistical error, of the energy in several cases and to validate our variational results. The full implementation of all numerical methods used is available in a public GitHub repository [23].

### A. System Hamiltonian

We consider a system inspired by the experimental setup of Ref. [17], where a Bose-Einstein condensate (BEC) is coupled to a single-mode optical cavity. The theoretical framework follows Refs. [24, 25], which generalize the Jaynes-Cummings in a rotating-wave and dipole approximation to many-body systems of ultracold atoms by treating both the cavity field and the atomic motion quantum mechanically.

Under adiabatic elimination of the electronically excited states and assuming the system reaches a steady state [17, 24, 25], the system can be described by an effective Hamiltonian of the form

$$\hat{H}_{\text{eff}} = \hat{H}_A + \hat{V}_{\text{int}}, \quad (1)$$

where  $\hat{H}_A$  accounts for the atomic kinetic energy, external trapping, and contact interactions, and  $\hat{V}_{\text{int}}$  describes the cavity-mediated long-range interactions.

The interaction potential takes the form

$$\begin{aligned} \hat{V}_{\text{int}} = V_0 \int d^3r d^3r' \hat{\Psi}^\dagger(\mathbf{r}) \hat{\Psi}^\dagger(\mathbf{r}') \cos(k_L x) \cos(k_L z) \\ \times \cos(k_L x') \cos(k_L z') \hat{\Psi}(\mathbf{r}) \hat{\Psi}(\mathbf{r}'), \end{aligned} \quad (2)$$

where  $\hat{\Psi}(\mathbf{r})$  is the bosonic field operator, and  $k_L = 2\pi/\lambda$  is the wavevector associated with the pump laser. The interaction strength  $V_0$  is given by  $V_0 \approx \hbar \frac{\eta^2}{\Delta_c - U_0 B_0}$ . Here,  $\eta$  is the two-photon Rabi frequency,  $\Delta_c$  is the detuning between the pump laser and cavity resonance,  $U_0$  is the single-atom light shift, and  $B_0$  is the mean-field expectation value of the bunching parameter in steady state.

Besides the interaction potential, the effective Hamil-

tonian contains an atomic contribution given by

$$\hat{H}_A = \int d^3 \mathbf{r} \hat{\Psi}^\dagger(\mathbf{r}) \left[ -\frac{\hbar^2 \nabla^2}{2m} + V_p \cos^2(k_L z) + \frac{g}{2} \hat{\Psi}^\dagger(\mathbf{r}) \hat{\Psi}(\mathbf{r}) \right] \hat{\Psi}(\mathbf{r}), \quad (3)$$

where  $V_p$  is the depth of the static optical lattice along  $z$ , and  $g = 4\pi\hbar^2 a/m$  is the coupling constant, characterizing the strength of interactions, described by the  $s$ -wave scattering length  $a$ .

The total effective Hamiltonian thus retains the kinetic and contact interaction terms of a conventional atomic system, but also incorporates a nonlocal interaction that is both periodic and long-ranged. Crucially, this interaction depends explicitly on the absolute position of atoms rather than their relative separations, thus breaking Galilean invariance. Due to the spatial structure inherited from the cavity and pump modes, atoms separated by integer multiples of the cavity wavelength interact identically, highlighting the infinite-range and periodic nature of the induced interactions.

### B. One-Dimensional Geometry

The full three-dimensional Hamiltonian Eq. (1) derived above serves as the starting point for our analysis. To make the simulations of the system properties more numerically tractable, we consider a simplified version of the many-body problem, in which the atomic motion is restricted to one dimension ( $x$ -axis). This approximation corresponds to the limit of a deep transverse optical lattice. In particular, a large lattice depth  $V_p$  in Eq. (3) freezes the atomic motion along the  $z$  direction, so that the separation between transverse energy levels becomes large and they cannot be excited, effectively reducing the system to two dimensions. A strictly one-dimensional geometry is then obtained by assuming an additional strong confinement in the remaining transverse direction, such that atomic motion is restricted to the  $x$  axis only.

The resulting effective one-dimensional Hamiltonian reads

$$H_{1D} = \sum_{i=1}^N \left( -\frac{\hbar^2}{2m} \frac{\partial^2}{\partial x_i^2} \right) + \sum_{i < j} V_0 \cos(k_L x_i) \cos(k_L x_j) + \sum_{i < j} g \delta(x_i - x_j), \quad (4)$$

where  $N$  is the number of atoms,  $g = -2\hbar^2/(ma_{1D})$  is the effective one-dimensional coupling constant, and  $a_{1D}$  is the one-dimensional  $s$ -wave scattering length. The second term in Eq. (4) describes a cavity-mediated long-range interaction with amplitude  $V_0$  and the wavevector  $k_L$ . To model repulsive contact interactions, we choose positive coupling constant  $g > 0$  which corresponds to negative scattering length,  $a_{1D} < 0$ .

The second term in Eq. (4) describes the cavity-mediated interaction. This interaction is of infinite range and unlike the contact interaction, it breaks translational invariance and imposes a spatial periodicity with wavevector  $k_L$ .

The underlying optical lattice sets natural units for the energy and length to compare with. We choose the cavity wavelength  $\lambda$  as the unit of length and define the natural energy scale as

$$\varepsilon = \frac{\hbar^2}{m\lambda^2},$$

which, up to a numerical factor  $(2\pi^2)$ , corresponds to the recoil energy  $E_r = \hbar^2 k_L^2 / (2m)$ .

### C. Exact wavefunction for two particles

To obtain the ground-state energy  $E_0$  and wavefunction  $\psi_2(x_1, x_2)$ , we solve the Schrödinger equation in imaginary time for two particles interacting via the cavity-mediated potential given by the second term of Eq. (4) in a one-dimensional box with periodic boundary conditions. We evolve the system in imaginary time by replacing  $t \rightarrow -i\tau/\hbar$  in the time-dependent Schrödinger equation. We start from a continuous normalized trial wavefunction  $\psi(x_1, x_2, \tau = 0)$  and numerically solve the Schrödinger differential equation.

As the imaginary time increases, higher-energy components decay faster than the ground-state component, and the wavefunction is projected to the ground-state of the Hamiltonian (up to normalization):

$$\psi(x_1, x_2, \tau) \xrightarrow{\tau \rightarrow \infty} \psi_2(x_1, x_2) e^{-E_0 \tau} \quad (5)$$

The resulting wavefunction is sampled on a discrete spatial grid and is interpolated using cubic B-splines. Fininf the exact solution of the two-body problem plays two major roles in our analysis, it provides physical insight into the two-body correlations induced by the cavity interaction, and it serves as a building block for constructing the many-body trial wavefunction we used in variational and diffusion Monte Carlo simulations.

### D. Trial Wavefunction for Many-Body Systems

To construct a trial wavefunction suitable for studying the many-body system, the standard approach is to use the pair-product Jastrow ansatz, which encodes pairwise correlations in homogeneous quantum systems,

$$\Psi_{\text{Jastrow}}(\mathbf{x}) = \prod_{i < j} f(|x_i - x_j|), \quad (6)$$

where the pairwise function  $f(|x_i - x_j|)$  depends only on the interparticle distance  $|x_i - x_j|$ , assuming translational invariance of the interaction potential. However,

TABLE I. Summary of trial wavefunctions for different interaction regimes and quantum statistics. ‘‘LR’’ refers to cavity-mediated long-range interactions (Second term of Eq. (4)), while ‘‘SR’’ denotes short-range contact interactions modeled by a delta-function potential. Symbols B and F indicate bosonic and fermionic symmetry, respectively. The factor  $\psi_2(x_i, x_j)$  represents the exact two-body wavefunction for the long-range interaction case. Here,  $k_L$  denotes the cavity wavevector and  $L$  the size of the system.

System	Trial wavefunction
Bosons LR	$\Psi_{\text{LR}}^{(\text{B})}(x_1, \dots, x_N) = \prod_{i < j} \psi_2(x_i, x_j)$
Bosons SR+LR	$\Psi_{\text{SR+LR}}^{(\text{B})}(x_1, \dots, x_N) = \prod_{i < j} \psi_2(x_i, x_j) \prod_{i < j} \cos[k_c( x_i - x_j  - \frac{L}{2})]$
Fermions LR	$\Psi_{\text{LR}}^{(\text{F})}(x_1, \dots, x_N) = \prod_{i < j} \psi_2(x_i, x_j) \prod_{i < j} \sin[\frac{\pi}{L}(x_i - x_j)]$
Fermions SR+LR	No contact interaction can be added because spinless fermions do not interact via <i>s</i> -wave scattering

in our case, the cavity-mediated interaction explicitly breaks translational invariance, and thus the standard Jastrow form (6) fails to adequately capture the physics of the interaction. Instead, we adopt a position-resolved ansatz based on the two-body wavefunction  $\psi_2(x_i, x_j)$  that depends on the positions of both particles

$$\Psi_{\text{position}}(\mathbf{x}) = \prod_{i < j} f(x_i, x_j). \quad (7)$$

This allows us to accurately capture the position-dependent correlations induced by the periodic long-range interaction.

### 1. Bosons with long-range interaction

We use the wavefunction  $\psi_2(x_i, x_j)$  of the exact (numerical) solution of the Schrödinger problem to build a trial many-body wavefunction for long-range interactions. Following the spirit of Jastrow-type wavefunctions, we extend the pairwise structure by taking the product over all pairs of particles,

$$\Psi_{\text{LR}}^{(\text{B})}(x_1, \dots, x_N) = \prod_{i < j} \psi_2(x_i, x_j). \quad (8)$$

This form allows us to retain the spatial correlations induced by the cavity-mediated interaction. Since the two-particle wavefunction depends on the positions of both particles rather than just their relative distance, Eq. (8) can capture the non-translationally-invariant structure for the many-body case.

However, wavefunction (8) only includes the cavity interaction. To be able to explore more relevant physical regimes, we consider two modifications of this wavefunction to account for (i) short-range contact interactions, (ii) fermionic statistics. These extra factors are multiplied into the wavefunction and can be added or not depending on the parameters we choose.

### 2. Bosons with short- and long-range interaction

To incorporate short-range repulsion, which is represented in Eq. (4) by a delta function we propose the following expression for the trial wavefunction

$$\Psi_{\text{SR+LR}}^{(\text{B})}(x_1, \dots, x_N) = \prod_{i < j} \psi_2(x_i, x_j) \times \prod_{i < j} f_{2B}(|x_i - x_j|), \quad (9)$$

where  $f_{2B}(|x|) = \cos[k_c(|x| - \frac{L}{2})]$ , which is chosen to satisfy the Bethe-Peierls boundary condition  $\left. \frac{f'_{2B}(x)}{f_{2B}(x)} \right|_{x \rightarrow 0} = -\frac{1}{a_{1D}}$  which allows us to include the effect of contact interactions without having to deal with the singular nature of the delta potential directly[26]. As well,  $f_{2B}(x)$  is chosen to satisfy the periodic boundary conditions, as  $f'_{2B}(\frac{L}{2}) = 0$ .  $L$  corresponds to the size of the 1D box and  $k_c$  is determined by the one-dimensional scattering length  $a_{1D}$  through the Bethe-Peierls boundary condition.

### 3. Fermions with long-range interaction

In addition to short-range repulsion, we also explore the effect of quantum statistics. More specifically, we compare our bosonic system to its fermionic counterpart. According to Bose-Einstein statistics, the many-body wavefunction must be symmetric under the exchange of any two particles. Indeed, wavefunctions (8) and (9) preserve bosonic symmetry, that is

$$\Psi_{\text{LR}}^{(\text{B})}(\dots, x_i, \dots, x_j, \dots) = \Psi_{\text{SLR}}^{(\text{B})}(\dots, x_j, \dots, x_i, \dots) \quad (10)$$

$$\Psi_{\text{SR+LR}}^{(\text{B})}(\dots, x_i, \dots, x_j, \dots) = \Psi_{\text{SR+LR}}^{(\text{B})}(\dots, x_j, \dots, x_i, \dots),$$

remain the same under the exchange of any two particles  $i$  and  $j$ , where  $N$  is the total number of particles in the system..

However, for Fermi-Dirac statistics, the many-body wavefunction must be antisymmetric under two-particle

exchange, which implies that

$$\Psi_{\text{LR}}^{(\text{F})}(\dots, x_i, \dots, x_j, \dots) = -\Psi_{\text{LR}}^{(\text{F})}(\dots, x_j, \dots, x_i, \dots) \quad (11)$$

To introduce the antisymmetrization of the wavefunction we consider the ground-state wavefunction of an ideal Fermi gas in the absence of interaction as a Slater determinant, which in one dimension takes the form of a Vandermonde determinant and can be written as a pair product

$$\begin{aligned} \Psi^{(\text{F})}(x_1, \dots, x_N) &= \frac{1}{\sqrt{N!}} \det [e^{ik_j x_i}]_{i,j=1}^N \\ &= \text{const} \times \prod_{i < j} \sin \left[ \frac{\pi}{L} (x_i - x_j) \right], \end{aligned} \quad (12)$$

where  $k_j = \frac{2\pi}{L} n_j$ , and the  $n_j$  are integers labeling the  $N$  lowest-energy single-particle states.

In order to take the long-range interactions into account, we use the following wavefunction to describe fermions,

$$\Psi_{\text{LR}}^{(\text{F})}(x_1, \dots, x_N) = \prod_{i < j} \psi_2(x_i, x_j) \prod_{i < j} \sin \left[ \frac{\pi}{L} (x_i - x_j) \right]. \quad (13)$$

This wavefunction vanishes whenever any two particles are at the same position, enforcing the nodal structure required for a system of spinless fermions.

### E. Quantum Monte Carlo Methods

To study the ground-state properties of the system, we employ Quantum Monte Carlo (QMC) techniques, which provide accurate non-perturbative estimates for strongly correlated systems. Specifically, we use variational Monte Carlo (VMC) method as the main tool for computing energetic and structural observables, and diffusion Monte Carlo (DMC) method for benchmarking our trial wavefunction in selected characteristic cases. These benchmarking results can be consulted in Appx. A.

#### 1. Observables

The main observable calculated in the many-body case is the ground-state energy. In addition to it, we compute a number of observables to describe spatial correlations in the system.

We calculated the density profile  $n(x)$  to quantify how particles are distributed within the box

$$n(x) = \frac{1}{N} \left\langle \sum_{i=1}^N \delta(x - x_i) \right\rangle \quad (14)$$

where brackets  $\langle \dots \rangle$  denotes the expectation value over the ground-state distribution.

We also calculate the pair distribution function  $g^{(2)}(x, x')$ , which measures the probability of finding a pair of particles one occupying  $x$  and the other  $x'$ , or vice versa.

$$g^{(2)}(x, x') = \frac{2}{N(N-1)} \left\langle \sum_{i < j} \delta(x - x_i) \delta(x' - x_j) \right\rangle. \quad (15)$$

Due to the absence of Galilean invariance,  $g^{(2)}(x, x')$  depends on two positions  $(x, x')$  and cannot be reduced to a function depending only on the relative positions  $(x - x')$ . This function captures short and long-range spatial correlations.

Finally, we calculate the Leggett bound[27] to quantify superfluid response. The Leggett bound provides an upper limit to the superfluid fraction,

$$\frac{\rho_S}{\rho} \leq \frac{1}{\langle n(x) \rangle \langle \frac{1}{n(x)} \rangle}, \quad (16)$$

where  $n(x)$  is the density profile defined in Eq. (14). These observables together allow us to interpret the energy results and identify signatures of localization, clustering, or ordering driven by the interaction parameters.

All Monte Carlo results carry statistical uncertainties inherent to the sampling process. These are estimated following the error bunching method explained in more detail in Ref. [28], but are typically smaller than the symbol size and thus not visible in the plots we show in this work.

## III. TWO PARTICLE ANALYSIS

Now that we have defined the full Hamiltonian and the numerical methods used throughout this study, we pass to the actual analysis of the system. We choose as a starting point the simplest case, two particles interacting only via long-range interactions and confined to a box with periodic boundary conditions. In this case we rely on the Imaginary Time Evolution (ITE) scheme to find the ground-state properties exactly.

Although seemingly trivial, the two-particle case is yet interesting for several reasons. On one hand, it represents the minimal setting in which long-range interaction appears, and thus, interesting physical behaviors emerge for the first time. On the other hand, the wavefunction of the two-particle solution is used in the construction of the wavefunction in the many-particle case.

### A. Wavefunction Structure and Symmetries

In order to study how the interactions affect the wavefunction structure, we show in Fig. 1 the interaction potential, and the resulting two-body wavefunction for characteristic cases with  $|V_0| = 10\epsilon$  and  $|V_0| = 100\epsilon$  in both the attractive,  $V_0 < 0$ , and repulsive,  $V_0 > 0$ , cases.

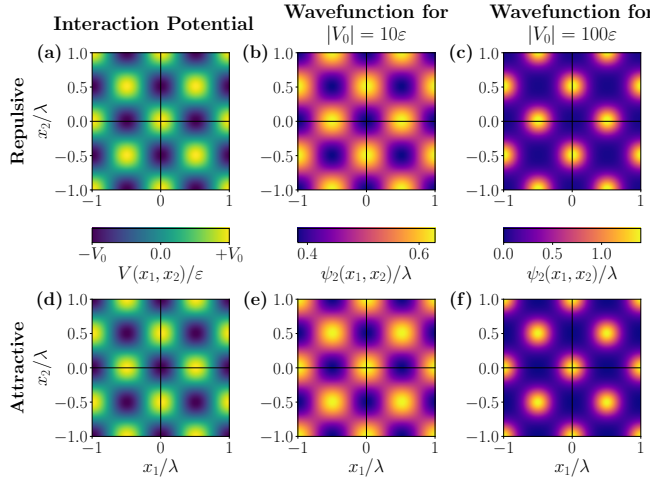


FIG. 1. Long-range interaction potential and two-body wavefunctions. Panels (a) and (d): cavity-mediated long-range interaction given by the second term of Eq. (4) for the repulsive and attractive cases, respectively. Panels (b) and (c): ground-state two-body wavefunction  $\psi(x_1, x_2)$  for repulsive interactions, obtained via imaginary time evolution, at interaction strengths  $V_0 = 10\epsilon$  and  $V_0 = 100\epsilon$ . Panels (e) and (f): ground-state two-body wavefunctions for the corresponding attractive case.

We find that a characteristic checkerboard pattern emerges. Remarkably, this pattern in the wavefunction is opposite to the pattern in the interactions, that is, maxima in the interaction, correspond to minima in the wavefunction, and vice versa. This result reflects the tendency of the system to minimize its energy by occupying the regions where the interaction between particles is minimal.

In addition, an important feature that already emerges in the two-particle case is the symmetry relating repulsive and attractive interactions. By comparing Fig. 1 (b) with (e) and Fig. 1 (c) with (f), one observes that the wavefunctions exhibit identical patterns, but shifted by half a period, following the property of the potential,

$$V(x_1, x_2) = -V\left(x_1 + \frac{\lambda}{2}, x_2\right) = -V\left(x_1, x_2 + \frac{\lambda}{2}\right). \quad (17)$$

In the attractive case, the diagonal ( $x_1 = x_2$ ) terms of the wavefunction are strongly populated, indicating that the two particles tend to occupy the same position, similarly to what happens for attractive short-range interactions. On the contrary, for long-range interactions, the shifted diagonals ( $x_1 = x_2 + \ell \cdot \lambda$ , with  $\ell = \pm 1, \pm 2, \dots$ ) are as well populated with the same weight. Physically, the interaction potential is attractive in regions, where the product of the cosine functions is positive, see the second term of Eq. (4). In contrast, in the repulsive case, the wavefunction is suppressed along the diagonal as the particles avoid each other and preferably occupy positions separated by half a period, where the product of cosines in the second term of Eq. (4) is negative. The

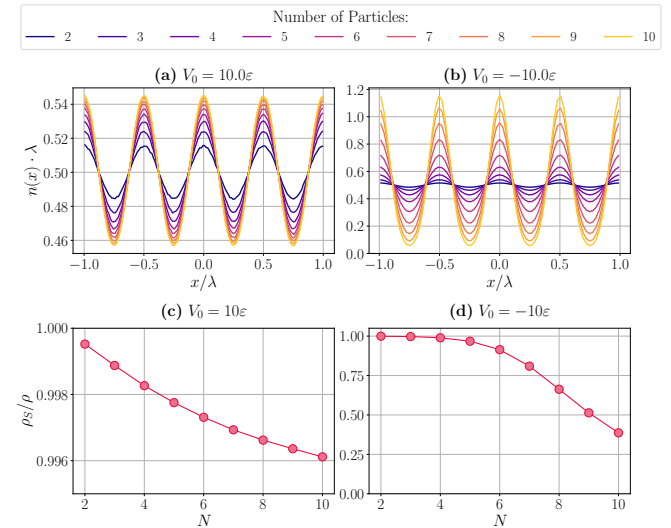


FIG. 2. Density profiles  $n(x)$  for various number of particles  $N = 2, \dots, 10$  obtained by Metropolis sampling, and the corresponding superfluid fraction estimated by the Leggett bound (16). The top row, panels (a) and (b), shows the density profiles  $n(x)$ , while bottom row, panels (c) and (d), displays the superfluid fraction  $\rho_s/\rho$ . The amplitude of  $n(x)$  increases with the number of particles  $N$ . Larger amplitude corresponds to systems with more particles, both for repulsive ( $V_0 > 0$ ) and attractive ( $V_0 < 0$ ) interactions. Panels (a) and (c): repulsive interactions with  $V_0 = 10\epsilon$ . Panels (b) and (d): attractive interactions with  $V_0 = -10\epsilon$ . All simulations are performed by fixing the length of the system to  $L = 2\lambda$  and changing the density as  $\rho = N/L$ .

way the system lowers its energy depends on the sign of the interaction, which in turn causes a shift in the characteristic pattern of the wavefunction.

In order to show how the amplitude  $V_0$  of the long-range interactions affects the wavefunction, we show in panels (b) and (c) of Fig. 1 the wave function for  $|V_0| = 10$  and 100. It becomes evident that higher amplitude of interactions leads to stronger localization of the particles within the interaction wells, both in the attractive and repulsive cases. In the limit of large  $V_0$ , the wavefunction fragments and resembles the ground-state of a harmonic oscillator repeated periodically across a grid of wells, following the structure of the cavity-mediated potential.

#### IV. GROUND-STATE PROPERTIES OF AN IDEAL BOSE GAS WITH CAVITY-MEDIATED INTERACTIONS

Using the VMC method, we analyze the ground-state properties of an ideal Bose gas subject exclusively to cavity-mediated long-range interactions, as described by the Hamiltonian Eq. (4) in the absence of short-range interactions, with  $g = 0$ . This simplified setting allows us to isolate the effects of the periodic, infinite-range interaction and examine its impact on observables such as the

density profile, superfluid response, and energy scaling.

### A. Density profile and superfluid response

The density profiles obtained from our Monte Carlo simulations are shown in panels Fig. 2 (a) and (b) and display periodic modulation for both attractive ( $V_0 < 0$ ) and repulsive ( $V_0 > 0$ ) interactions. These modulations reflect the underlying periodicity of the cavity-mediated interaction and break the continuous translational invariance that exists in the non-interacting Bose gas ( $V_0 = 0$ ). Throughout this analysis, we consider systems of fixed length equal to  $L = 2\lambda$ .

For larger number of particles, the peaks in the density become higher, signaling stronger localization, both for attractive and repulsive interactions, although the effect is significantly stronger for attractive interactions. In the repulsive case, the valleys between peaks remain finite, suggesting that particles stay delocalized across the system, eventually resulting in a coherent system. In contrast, in the attractive case, minimal density rapidly approaches zero, indicating a tendency of the system to fragment and to lose coherence.

Remarkably, attractive interactions have different consequences for short-range and long-range interactions. Bosons with short-range interactions described by scattering length  $a$  form bright solitons [29] where all particles form a deeply bound state of size  $\xi \propto a/N$ . The resulting density in the position of the center of mass of the soliton rapidly grows as the number of particles is increased,  $n(0) \propto N/\xi \propto N^2/a$ . Strictly speaking, the average density is constant due to the Galilean invariance as the soliton can be located at any point. Instead, for long-range interactions, the Galilean invariance is broken and the density depends on position. Most importantly, there is a series of localized states, rather than a single bound state, following the symmetry of the interaction potential. A less trivial property difference is that while for attractive contact interactions all bosons bind together, so that by adding another bosons to present  $N$  ones, most probably it will be found in the vicinity of position of the soliton (i.e. position of the center of mass), for long-range interactions even of all  $N$  particles stay in the same site (minimum of the interaction potential), next particle can stay with the same probability at the same site or in any different site.

Instead, the ground-state is a symmetric superposition across equivalent minima. The result is a clustered but delocalized phase that does not reach full crystallization. Throughout this paper, we refer to this phase as *delocalized bound state* making a reference to its being a bound state (characterized by large negative energy and highly peaked narrow density profile) as well as being delocalized (instead of a single peak, there are many peaks all over the box).

In the repulsive regime, the system also develops periodic density, but the particles remain connected across

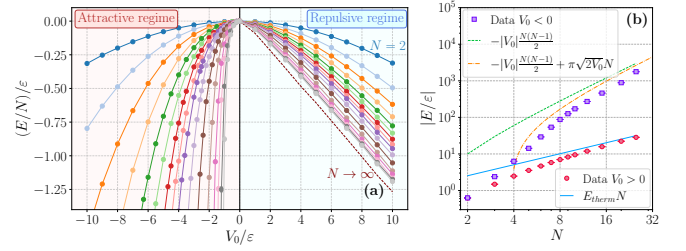


FIG. 3. Ground-state energy of bosons interacting via cavity-mediated long-range potential. Symbols show VMC results. Panel (a): energy per particle  $E/N$  as a function of interaction strength  $V_0$  for various particle numbers  $N = \{2, 3, 4, 5, 6, 7, 8, 9, 10, 12, 15, 20, 25, 30, 35, 40\}$ . In the repulsive case ( $V_0 > 0$ ), an extrapolated estimate of the thermodynamic limit is shown as a dashed maroon line. In contrast, the attractive case ( $V_0 < 0$ ) leads to a divergent energy. Panel (b): Absolute value of the energy,  $|E|$ , for the specific case of  $|V_0| = 10\varepsilon$  as a function of the number of particles,  $N$ , for both interaction signs, compared to the asymptotic scalings law: Eq. (21) for the attractive case, and  $E_{th}N$  for the repulsive one. All simulations are performed at constant density  $\rho = 1\lambda^{-1}$  and changing the length  $L = N/\rho$ .

the system, suggesting a modulated but coherent phase.

Given the presence of periodic modulation, one might expect suppressed coherence in the system. However, the persistence of coherence, particularly in the repulsive regime, suggests the possible presence of superfluidity. To quantify it, we compute the superfluid fraction with Eq. (16) and using the density profiles shown in Fig. 2 (a) and (b).

The superfluid response is very different in the attractive and repulsive cases (note the different vertical scales in Fig. 2 (c) and (d)). Indeed, in the attractive regime, the superfluid fraction rapidly decays with increasing  $N$ , consistent with the idea that particles localize around the potential minima and lose phase coherence. On the other hand, the repulsive regime retains a finite superfluid fraction for large  $N$ , consistent with a delocalized phase that forms a supersolid.

### B. Energy and thermodynamic behavior

In order to characterize the properties in approaching the thermodynamic limit, we study how the energy scales with both particle number  $N$  and interaction strength  $V_0$ , keeping the density fixed at  $\rho = 1\lambda^{-1}$ . Figure 3 (a) reports the energy per particle  $E/N$  as a function of  $V_0$ , while Fig. 3 (b) displays the total energy  $E(N)$  as a function of the number of particles for fixed  $|V_0| = 10\varepsilon$ .

In the absence of long-range interaction,  $V_0 = 0$ , we recover the trivial result for a homogeneous ideal Bose gas,

$$E = 0. \quad (18)$$

As the long-range interaction is introduced, the energy,

$E$ , becomes negative both in the attractive and repulsive regimes, reflecting the formation of correlated states in the regions where the interaction potential is negative. While this lowering of energy is often associated with spatial clustering, in this case, the particles remain delocalized and distribute themselves across the periodic minima of the cavity-mediated potential.

For  $N = 2$  particles, the energy decreases as the amplitude of the interaction  $|V_0|$  is increased, however the resulting energy is exactly the same for repulsive and attractive interactions of the same strengths, i.e, for amplitudes  $\pm V_0$ . This property was anticipated in Sec. III, where we discussed that in the two-particle case both solutions have similar wavefunctions, but displaced in space, and share the same energy. Instead, by increasing further the number of particles, the system properties become drastically different between repulsive and attractive cases.

In the repulsive regime,  $V_0 > 0$ , we observe that in the limit of large number of particles, the energy per particle converges toward a constant value,

$$\lim_{N \rightarrow \infty} \frac{E(N)}{N} = \text{const}, \quad (19)$$

indicating that the system energy is extensive and possesses a well-defined thermodynamic limit. To extract the thermodynamic energy, we perform a linear extrapolation of  $E/N$  versus  $1/N$  for each value of  $V_0$ , with the intercept at  $1/N = 0$  corresponding to the infinite-particle limit. The extrapolation to the thermodynamic limit is shown in Fig. 3 (a) as the dashed maroon line.

In Fig. 3 (b) we show the dependence of the absolute value of the ground-state energy on the number of particles in two characteristic cases,  $V_0 = 10\epsilon$  (repulsion) and  $V_0 = -10\epsilon$  (attraction). In the repulsive case, the energy grows linearly with particle number, consistent with extensive behavior. This confirms the stability of the gas state and supports the thermodynamic analysis above.

In contrast, the attractive regime exhibits markedly different behavior. As seen in Fig. 3 (a) and (b), the energy per particle continues to decrease without any saturation

$$\frac{E(N)}{N} \rightarrow -\infty, \quad (20)$$

and no thermodynamic limit is reached. This behavior is characteristic of collapse, particles bunch together into the periodic minima of the interaction potential, and the interaction energy dominates. In the large- $N$  limit, the particles are highly localized in the vicinity of the minima, and the ground-state energy approaches the zero temperature energy of a classical system, given by

$$E_{\text{int}}^{\text{clas}}(N) = -|V_0| \frac{N(N-1)}{2}. \quad (21)$$

Nonetheless, the total energy remains less negative than this pure interaction scaling, indicating that kinetic

energy still plays a non-negligible role in moderating the collapse. While in a classical system at zero temperature, the particles freeze in the minimum of the potential energy, a quantum system cannot do that due to the Heisenberg uncertainty principle. Quantum fluctuations lead to a finite kinetic energy and an additional increase of the potential energy. The first correction due to the quantum fluctuations can be approximated by the ground-state energy of a harmonic oscillator,

$$E = -|V_0| \frac{N(N-1)}{2} + N \frac{\hbar\omega_0}{2} + \dots, \quad (22)$$

where the level spacing  $\omega_0$  is obtained by the harmonic approximation of the minimum of the interaction potential:

$$\begin{aligned} V_0 \cos^2 \left( \frac{2\pi}{\lambda} x \right) &\approx V_0 \left( \frac{2\pi}{\lambda} \right)^2 \left( x - \frac{\lambda}{4} \right)^2 \\ &= \frac{1}{2} m \omega_0^2 \left( x - \frac{\lambda}{4} \right)^2. \end{aligned} \quad (23)$$

This correction is shown in Fig. 3 (b) as the orange dashed line. We observe a slight improvement, as the resulting energy is lower than the previous approximation. However, higher-order corrections should be considered, since the behavior is still not fully captured.

Together, the results in Fig. 3 (a) and (b) highlight a clear contrast, the repulsive regime remains stable and extensive, while the attractive regime exhibits super-extensive scaling and collapse. This behavior is a direct consequence of the all-to-all character of the cavity-mediated interaction potential.

## V. EFFECTS OF SHORT-RANGE INTERACTIONS ON CAVITY-MEDIATED SYSTEMS

To study the effects of cavity-mediated long-range interactions, we explore quantum many-body systems incorporating either short-range contact interactions or fermionic statistics. Using Variational Monte Carlo (VMC) method, we calculate observables such as the ground-state energy, density profiles, pair correlation functions, and the static structure factor. These quantities allow us to characterize how the interplay between short-range and cavity-mediated long-range interactions modifies the system physical behavior and stability.

To establish benchmarks, we consider two well-understood limits in the absence of cavity-mediated interactions, a weakly interacting Bose gas with short-range repulsion and an ideal Fermi gas governed solely by quantum statistics. The weakly interacting Bose gas is accurately described by the Lieb–Liniger model, whose exact solution through the Bethe ansatz provides access to ground-state energies and correlations at all interaction strengths.

Properties of a Bose system in the absence of long-range interactions are governed by the dimensionless Lieb–Liniger parameter  $\gamma = \frac{2}{\rho_0|a_{1D}|}$ , where  $\rho_0 = N/L$  denotes the average particle density. The parameter  $\gamma$  controls the crossover from weak ( $\gamma \ll 1$ ) to strong repulsion ( $\gamma \gg 1$ ), the former corresponds to the Gross–Pitaevskii regime, while the latter approaches the Tonks–Girardeau limit of impenetrable bosons. Our simulations focus on a weakly interacting regime with a coupling strength  $g = -\lambda/a_{1D} = 1.0$ , corresponding to  $\gamma = 2$  at unit density ( $\rho_0 = 1\lambda^{-1}$ ).

On the other hand, the ideal Fermi gas represents the non-interacting limit of a fermionic system, where the Pauli exclusion principle effectively acts as repulsive interaction. At low energies, both bosonic and fermionic systems are encompassed by the universal framework of Luttinger liquid theory [30–32], which captures common properties such as phononic excitations and algebraically decaying correlations, but with different Luttinger parameters.

By comparing these well-established cases with our full model, where both short-range and cavity-mediated infinite-range interactions are present, we gain insight into how the periodic long-range potential alters fundamental properties such as the superfluid response, and the structure factor. This comparative analysis helps us interpret deviations from ideal behavior in terms of emergent correlations and the competition between interaction scales, providing a deeper understanding of the stability and phases of cavity-mediated quantum systems.

### A. Density Profile and Frustrated Ordering

We begin by analyzing the density profiles  $n(x)$  and two-body correlation functions  $g^{(2)}(x_1, x_2)$  in the presence of short-range repulsion, either from contact interaction or Fermi statistics. In the repulsive regime ( $V_0 > 0$ ), both the cavity-mediated and short-range interactions discourage particles from occupying nearby positions. As expected, the density profiles remain relatively flat, with weak periodic modulations slightly softened by repulsion.

In Fig. 4 we show the density profile both for a system with contact interaction and a fermionic system. It is quite remarkable to see how, in the fermionic case, the behavior of the density profile is not as directly analogous to the purely long-range interaction case as it is for the contact interaction case. Although both fermions and the cavity-mediated interaction introduce a repulsive type of constraint, there is a competition, the system tends to behave more gas-like and lose the periodicity enforced by the cavity potential. This effect is more pronounced in the attractive regime (discussed further below), but it arises from the same fundamental mechanism.

For instance, when  $V_0 = -10\epsilon$ , the cavity-mediated interaction becomes less dominant as the particle number increases, allowing the fermionic repulsion to push the system toward a Fermi-gas-like configuration, though

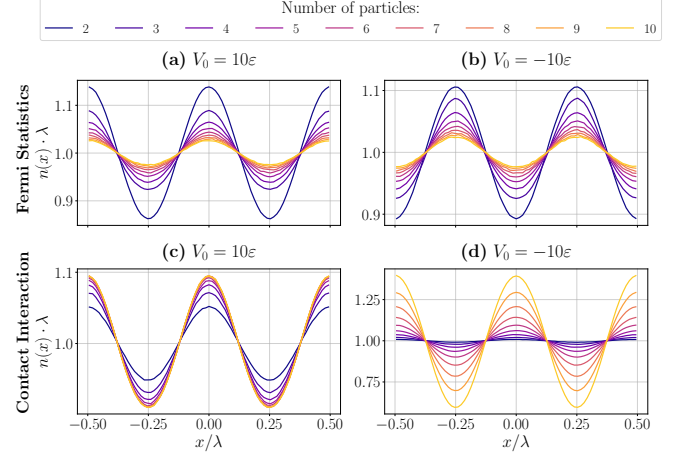


FIG. 4. Density profiles in the presence of short-range correlations for particle numbers  $N = 2, \dots, 10$ . Panel (a): fermionic system with repulsive long-range interaction ( $V_0 > 0$ ). Panel (b): fermionic system with attractive long-range interaction ( $V_0 < 0$ ). Panel (c): bosonic system with contact interaction  $\gamma > 0$  and repulsive long-range interaction. Panel (d): bosonic system with contact interaction and attractive long-range interaction. All simulations are performed by fixing the length of the system  $L = \lambda$  and changing the density  $\rho = N/L$ .

still retaining some imprint of the periodic potential. In the bosonic case with contact interaction, a similar effect could arise; however, the contact repulsion is much weaker than the cavity interaction, so the system behaves nearly identically to the ideal Bose gas with only long-range interactions.

The situation becomes more interesting in the attractive regime ( $V_0 < 0$ ), where the cavity-mediated interaction tends to localize particles in its potential minima, while short-range repulsion resists clustering. This competition creates frustration between the two interactions.

It is worth emphasizing that frustration only emerges in the many-body setting, and under our assumed system size  $L = \lambda$ . In larger systems, frustration tends to appear only at higher particle numbers, since the additional space provides more freedom to satisfy interaction constraints. The onset of frustration therefore depends not only on the number of particles but also on the system size, which together determine whether all pairwise constraints can be simultaneously fulfilled.

To explore this effect in detail, we focus on the fermionic system with  $N = 5$  particles—a size large enough to exhibit spatial structure, but small enough to resolve individual correlations. We choose the fermionic case because the effects of frustration are visually more pronounced due to the strong Pauli repulsion. Similar effects are also present in bosonic systems with contact interactions, though they are significantly weaker and harder to visualize with the same clarity.

Figure 5 shows both the density profile and the two-body correlation function for increasing attractive

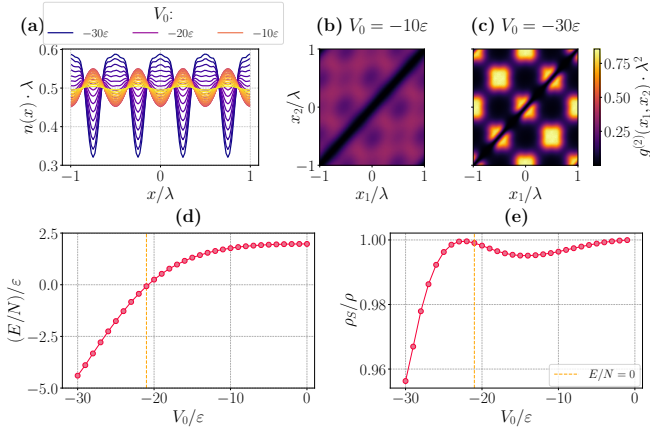


FIG. 5. Results for a spinless fermionic system with  $N = 5$  particles and attractive cavity-mediated interactions. Panel (a): density profile  $n(x)$  for varying  $V_0$ , exhibiting a shift at weak coupling and recovering the bosonic periodic structure at strong coupling Panels (b) and (c): two-body correlation function  $g^{(2)}(x_1, x_2)$  for  $V_0 = -10.0 \varepsilon$  and  $V_0 = -30.0 \varepsilon$ , respectively. Panel (d): energy per particle  $E/N$  as a function of  $V_0$ , showing a zero crossing. Panel (e): superfluid fraction obtained from the Leggett bound, Eq. (16), indicating a crossover in the superfluid response. All simulations are performed by fixing the system size  $L = 2\lambda$  and changing the density  $\rho = N/L$ .

strength. Panel (a) reveals that for moderate attraction ( $1 < |V_0|/\varepsilon < 20$ ), the density remains nearly uniform, though faint modulations emerge due to the underlying cavity-mediated interaction.

This effect becomes even clearer when observing the two-body correlation function  $g^{(2)}(x_1, x_2)$  in Fig. 5 (b). At  $V_0 = -10\varepsilon$ , which corresponds to an intermediate attraction, the pair distribution presents a very uniform pattern, but with a faint periodic modulation that has maxima now at the zeros of the interaction instead of the minima, corresponding to a half-period phase shift in the density profile, see Fig. 5 (a). The system avoids both the interaction maxima and the diagonal  $x_1 = x_2$ , which is forbidden by Fermi statistics.

This results in a frustrated arrangement that balances both types of interaction: the attractive cavity-mediated potential, which favors clustering, and the Pauli exclusion principle, which prevents particle overlap. As a result, the particles tend to organize near the zeros of the interaction potential, reflecting a nontrivial compromise between these opposing tendencies.

As  $|V_0|$  increases further, the periodic structure imposed by the cavity-mediated interaction begins to dominate. The system crystallizes into density maxima that align with the minima of the interaction potential, similar to what is observed in the long-range-only case. However, even in this limit, the system continues to avoid the diagonal in  $g^{(2)}$ , preserving Pauli exclusion. The width of this forbidden region narrows as the attraction grows stronger, reflecting increased localization around the cav-

ity minima and the growing dominance of the cavity-mediated interaction, Fig. 5 (a) and (c) for  $V_0 < -30\varepsilon$ , where the peak positions match those of the long-range-only case.

This frustrated regime, where particles are caught between the ordering tendency of the long-range interaction and the repulsive constraint imposed by Fermi statistics, defines a nontrivial configuration, neither an ideal Fermi gas nor the delocalized bound state found in the purely long-range Bose case. To quantify and further characterize the transition out of this regime, we compute both the energy per particle  $E/N$  and the Leggett upper bound for the superfluid fraction as functions of interaction strength.

The superfluid fraction is expected to remain finite as long as the system retains a delocalized, gas-like character, and to drop rapidly to zero once the particles begin to localize within the cavity minima. This makes it a useful indicator of the crossover between the frustrated regime and the interaction-dominated, symmetry-broken state.

As shown in Fig. 5 (d) and (e), the superfluid response remains large in the frustrated regime and becomes strongly suppressed once the long-range attraction becomes dominant. This crossover occurs just before the energy per particle turns negative ( $E/N < 0$ ), signaling the onset of a many-body bound state and ending the frustrated regime.

## B. Energy Scaling and Qualitative Phase Diagram

We now extend the energy analysis to systems that include additional short-range repulsion, either through Fermi statistics or weak contact interaction.

For strong long-range interactions, the observed behavior closely resembles that of the purely long-range case. In the repulsive regime,  $V_0 > 0$ , the energy per particle  $E/N$  converges with increasing  $N$ , confirming the existence of a well-defined thermodynamic limit. In the attractive regime,  $V_0 < 0$ , the energy decreases with  $N$  and shows signs of collapse, although the rate of divergence is reduced due to the presence of repulsive effects.

The most notable difference is found at  $V_0 = 0$ , where the energy is no longer zero but reflects the baseline contribution from the short-range terms. In the fermionic case, this corresponds to the energy of the ideal Fermi gas, which is significantly higher. In the bosonic case with contact interaction, the shift is much smaller, consistent with the weaker repulsion.

Importantly, the short-range repulsion acts to delay the onset of collapse. This stabilization is especially visible in the fermionic case, where Pauli repulsion remains strong even as  $V_0$  becomes increasingly negative. For bosons with contact interaction, the effect is much weaker, and for the same  $V_0$  as in the fermionic case, it is only noticeable at small  $N$ , where the relative contribution of the short-range repulsion to the total energy

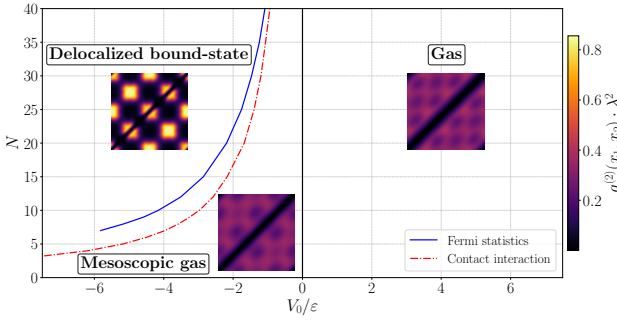


FIG. 6. Qualitative phase diagram showing three regimes: delocalized bound state, mesoscopic gas, and gas phase. The mesoscopic gas is separated from the thermodynamically stable gas phase by the vertical line  $V_0 = 0$ , and from the delocalized bound state by the line  $E/N = 0$ . For purely cavity-mediated long-range interactions, the  $V_0 = 0$  line marks the boundary between the gas and delocalized bound state. Representative pair correlation functions  $g^{(2)}(x_1, x_2)$  illustrate the changes in spatial correlations across these regimes. Simulations are performed at fixed density  $\rho = 1/\lambda$  with system size  $L = N/\rho$ , except for the pair correlation functions, which are computed at fixed  $L = 2\lambda$  for better visualization.

is larger before the long-range attraction dominates. As such, while the overall instability of the attractive regime persists, its onset is significantly modified by the nature and strength of short-range repulsion.

In the previous section, we identified the emergence of a frustrated regime when contact interactions are introduced and the system satisfies  $E/N > 0$ . We observed that the transition between different regimes occurs at the point where  $E/N \approx 0$ , which allowed us to determine the zero-crossings of the energy curves obtained for these two systems. Based on this criterion, Fig. 6 presents a qualitative phase diagram constructed by identifying the values of  $V_0$  at which  $E/N = 0$ , which we interpret as indicative of a change in the behavior of the system.

This phase diagram reveals three distinct regimes. In the repulsive case ( $V_0 > 0$ ), the system remains gas-like across all interaction strengths, exhibiting only a weak periodic modulation induced by the long-range interaction. In the attractive regime ( $V_0 < 0$ ), two qualitatively different phases emerge. For small values of  $V_0$ , the system remains in a mesoscopic gas phase: the LR attraction is not sufficiently strong to induce localization in the minima of the interaction potential, and the particles remain delocalized, exhibiting gas-like behavior. However, beyond a certain critical value of  $V_0$ , which depends on the particle number, the system localizes in the minima of the interaction potential, forming what we define as a delocalized bound state. It is important to point out that the gas-like phase for attractive interactions is a mesoscopic one, that is it exists only for a finite number of particles and vanishes in the thermodynamic limit. By increasing the number of particles, the system enters the delocalized bound state identified in the long-range-only

case and gradually loses all superfluid response.

We also observe that, in the presence of contact interactions, the critical amplitude  $V_0$  required for localization is lower than in the fermionic case. This difference can be attributed to the weaker effective repulsion between bosons with contact interactions, making the system more susceptible to clustering under attractive long-range forces.

## VI. CONCLUSIONS AND OUTLOOK

This paper studies the ground-state properties of a one-dimensional quantum system with cavity-mediated long-range interactions in continuous space, using numerical methods across different interaction regimes and quantum statistics. The system displays a rich variety of behaviors as summarized in the phase diagram

We investigate the many-body properties in the absence of short-range interactions, isolating the effects of cavity-mediated long-range potentials. Such a system exhibits two qualitatively different regimes depending on the sign of the interaction strength. For attractive interactions, particles strongly cluster at the periodic minima of the potential, leading to pronounced density modulations, a vanishing superfluid fraction, and the absence of a well-defined thermodynamic limit, we refer to this regime as a delocalized bound state. In contrast, repulsive long-range interactions produce a delocalized phase characterized by weak periodic density modulations, finite superfluid fraction, and a well-defined thermodynamic limit.

The incorporation of short-range repulsion, through either contact interactions or fermionic statistics, significantly modifies the properties of the system. The cavity-mediated interactions only weakly perturb the low-energy excitations in this regime. Instead, the interplay between long-range attraction and short-range repulsion generates a frustrated mesoscopic phase marked by intricate spatial correlations and a finite superfluid fraction. As attraction is increased further, the system undergoes a transition into a delocalized bound state phase, reflecting a rich competition between the repulsive forces and clustering tendencies.

From a methodological point, we developed a many-body trial wavefunction based on the exact two-body solution of the cavity-mediated potential. This wavefunction was implemented within both Variational Monte Carlo (VMC) and Diffusion Monte Carlo (DMC) methods. We validated these methods by benchmarking against known analytical limits (perturbative expansions), exactly solvable cases (ideal Fermi gas, Bethe ansatz for Lieb-Liniger gas) and other numerical methods (imaginary-time propagation for two-particle case), ensuring consistency across different interaction regimes. Additionally, convergence tests were performed with respect to simulation parameters such as particle number, time step size, and projection time, confirming the

robustness and accuracy of our approach. These validations guarantee reliable quantitative predictions for ground-state energies and correlation functions in cavity-mediated many-body systems.

The numerical methods developed here are versatile and can be extended to higher-dimensional or more realistic versions of the cavity-mediated model studied in this work. In particular, one could first consider the limit of a deep transverse lattice ( $V_p \rightarrow \infty$ ), freezing motion along  $z$  and reducing the system to two dimensions, and then further extend the approach to the full three-dimensional geometry, both corresponding to the actual experimental setup of Ref. [17]. Additionally, extra terms such as optical lattices, multimode cavity fields, or other position-dependent interactions can be incorporated within the same framework.

In conclusion, this study combines a physically motivated model with flexible numerical tools to explore a range of rich many-body phenomena. It offers both a foundation for future simulations and concrete insight into the behavior of ultracold atoms coupled to cavity fields.

## ACKNOWLEDGMENTS

This work has been funded by Grant PID2023-147475NB-I00 funded by MECI/AEI/10.13039/501100011033 and FEDER, UE, by grants 2021SGR01095 from Generalitat de Catalunya, and by Project CEX2019-000918-M of ICCUB (Unidad de Excelencia María de Maeztu). G.E.A. acknowledges the support of the Spanish Ministry of Science and Innovation (MCIN/AEI/10.13039/501100011033, grant PID2023-147469NB-C21), the Generalitat de Catalunya (grant 2021 SGR 01411) and Barcelona Supercomputing Center MareNostrum (FI-2025-1-0020). A.R-F. acknowledges additional funding from the Okinawa Institute of Science and Technology Graduate University.

## Appendix A: Comparing energy results using VMC and DMC methods

Figure 7 compares the ground-state energies obtained using Variational Monte Carlo (VMC) and Diffusion Monte Carlo (DMC) for different interaction regimes.

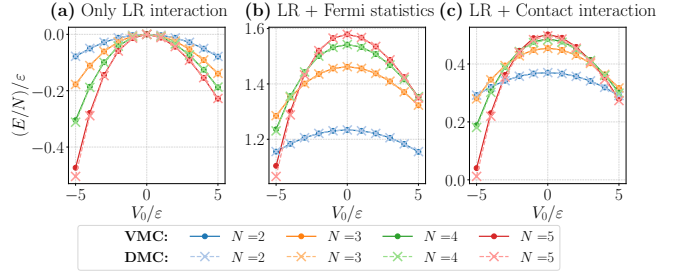


FIG. 7. Comparison of the energy obtained using Variational Monte Carlo (VMC) with the trial wavefunction specified in Table I, and the energy obtained using Diffusion Monte Carlo (DMC) using the same wavefunction as the guiding function. Panel (a): Long-range interaction only. Panel (b): Combined contact and long-range interactions. Panel (c): Long-range interaction with fermionic statistics.

In all panels, the same trial wavefunction (summarized in Table I) is used for both methods, serving as the variational ansatz in VMC and as the guiding function in DMC. As expected, the DMC energies are systematically lower than the VMC ones, in agreement with the variational principle. The energy difference provides an estimate of the quality of the trial wavefunction.

In the purely long-range case Fig. 7 (a), the two methods yield very similar results, indicating that the trial wavefunction accurately captures the dominant correlations. The discrepancy becomes more pronounced in the presence of contact interactions Fig. 7 (b), suggesting that short-range correlations are not fully described by the variational ansatz. In the fermionic case Fig. 7 (c), the fixed-node constraint is imposed by the nodal structure of the guiding wavefunction, and the observed energy difference reflects both the quality of this constraint and the accuracy of the trial state.

In general, as the number of particles increases, the VMC energy deviates more from the DMC result. This deviation also grows with increasing interaction strength  $V_0$ , particularly in the attractive regime, where the many-body behavior becomes more complex. Nevertheless, the VMC calculations still provide a qualitatively accurate description of the system, capturing the main features of density profiles, correlations, and trends in the ground-state energy. The DMC results serve as a benchmark, validating the reliability of the trial wavefunction and confirming that the combined VMC-DMC approach employed throughout this work yields robust and accurate predictions for both qualitative and quantitative aspects of the cavity-mediated many-body system.

---

[1] M. Greiner, O. Mandel, T. Esslinger, T. W. Hänsch, and I. Bloch, *Nature* **415**, 39 (2002).  
[2] D. Porras and J. I. Cirac, *Physical Review Letters* **92**, 207901 (2004).  
[3] M. Lewenstein, A. Sanpera, V. Ahufinger, B. Damski, A. Sen(De), and U. Sen, *Advances in Physics* **56**, 243 (2007).  
[4] C. Gross and I. Bloch, *Science* **357**, 995 (2017).  
[5] I. Bloch, J. Dalibard, and W. Zwerger, *Rev. Mod. Phys.* **80**, 885 (2008).

[6] C. Chin, R. Grimm, P. Julienne, and E. Tiesinga, *Rev. Mod. Phys.* **82**, 1225 (2010).

[7] D. Jaksch, C. Bruder, J. I. Cirac, C. W. Gardiner, and P. Zoller, *Phys. Rev. Lett.* **81**, 3108 (1998).

[8] M. Boninsegni and N. V. Prokof'ev, *Reviews of Modern Physics* **84**, 759 (2012).

[9] T. Lahaye, C. Menotti, L. Santos, M. Lewenstein, and T. Pfau, *Reports on Progress in Physics* **72**, 126401 (2009).

[10] M. A. Baranov, M. Dalmonte, G. Pupillo, and P. Zoller, *Chemical Reviews* **112**, 5012 (2012).

[11] H. Ritsch, P. Domokos, F. Brennecke, and T. Esslinger, *Rev. Mod. Phys.* **85**, 553 (2013).

[12] F. Mivehvar, F. Piazza, T. Donner, and H. Ritsch, *Advances in Physics* **70**, 1 (2021), <https://doi.org/10.1080/00018732.2021.1969727>.

[13] D. Nagy, G. Szirmai, and P. Domokos, *The European Physical Journal D* **48**, 127 (2008).

[14] A. Vukics, J. Janszky, and P. Domokos, *Journal of Physics B: Atomic, Molecular and Optical Physics* **38**, 1453 (2005).

[15] A. T. Black, H. W. Chan, and V. Vuletić, *Physical Review Letters* **91**, 203001 (2003).

[16] S. Gopalakrishnan, B. L. Lev, and P. M. Goldbart, *Phys. Rev. A* **82**, 043612 (2010).

[17] R. Mottl, F. Brennecke, K. Baumann, R. Landig, T. Donner, and T. Esslinger, *Science* **336**, 1570 (2012).

[18] R. Landig, L. Hruby, N. Dogra, M. Landini, R. Mottl, T. Donner, and T. Esslinger, *Nature* **532**, 476 (2016).

[19] J. Klinder, H. Keßler, M. Wolke, L. Mathey, and A. Hemmerich, *Proceedings of the National Academy of Sciences* **112**, 3290 (2015).

[20] J. Vijayan, J. Piotrowski, C. Gonzalez-Ballester, K. Weber, O. Romero-Isart, and L. Novotny, *Nature Physics* **20**, 859 (2024).

[21] N. Dogra, F. Brennecke, S. D. Huber, and T. Donner, *Physical Review A* **94**, 023632 (2016).

[22] P. Karpov and F. Piazza, *Physical Review Letters* **128**, 103201 (2022).

[23] M. Dominguez-Navarro, Quantum Monte Carlo study of systems interacting via long-range interactions mediated by a cavity (TFM-2025), [https://github.com/martadomin/Cavity-mediated\\_interaction\\_TFM](https://github.com/martadomin/Cavity-mediated_interaction_TFM), accessed: 2025-07-06.

[24] C. Maschler and H. Ritsch, *Physical Review Letters* **95**, 260401 (2005).

[25] C. Maschler, I. B. Mekhov, and H. Ritsch, *The European Physical Journal D* **46**, 545 (2008).

[26] H. Bethe and R. Peierls, *Proceedings of the Royal Society of London. A. Mathematical and Physical Sciences* **148**, 146 (1935).

[27] A. J. Leggett, *Journal of Statistical Physics* **93**, 927 (1998).

[28] H. Flyvbjerg and H. G. Petersen, *The Journal of Chemical Physics* **91**, 461–466 (1989).

[29] J. B. McGuire, *Journal of Mathematical Physics* **5**, 622 (1964).

[30] F. D. M. Haldane, *Journal of Physics C: Solid State Physics* **14**, 2585 (1981).

[31] M. A. Cazalilla, R. Citro, T. Giamarchi, E. Orignac, and M. Rigol, *Reviews of Modern Physics* **83**, 1405 (2011).

[32] M. A. Cazalilla, *Journal of Physics B: Atomic, Molecular and Optical Physics* **37**, S1 (2004).